ACS OMEGA

http://pubs.acs.org/journal/acsodf

Article

Effect of Diel Cycling Temperature, Relative Humidity, and Synthetic Route on the Surface Morphology and Hydrolysis of α-U_3O_8

Alexa B. Hanson, Cody A. Nizinski, and Luther W. McDonald, IV*

Cite This: *ACS Omega* 2021, 6, 18426−18433

Read Online

ACCESS | Metrics & More | Article Recommendations | Supporting Information

ABSTRACT: The speciation and morphological changes of α-U_3O_8 following aging under diel cycling temperature and relative humidity (RH) have been examined. This work advances the knowledge of U-oxide hydration as a result of synthetic route and environmental conditions, ultimately giving novel insight into nuclear material provenance. α-U_3O_8 was synthesized via the washed uranyl peroxide (UO_4) and ammonium uranyl carbonate (AUC) synthetic routes to produce unaged starting materials with different morphologies. α-U_3O_8 from UO_4 is comprised of subrounded particles, while α-U_3O_8 from AUC contains blocky, porous particles approximately an order of magnitude larger than particles from UO_4. For aging, a humidity chamber was programmed for continuous daily cycles of 12 "high" hours of 45 °C and 90% RH, and 12 "low" hours of 25 °C and 20% RH. Samples were analyzed at varying intervals of 14, 24, 36, 43, and 54 days. At each aging interval, crystallographic changes were measured via powder X-ray diffraction coupled with whole pattern fitting for quantitative analysis. Morphologic effects were studied via scanning electron microscopy and 12-way classification via machine learning. While all samples were found to have distinguishing morphologic characteristics (93.2% classification accuracy), α-U_3O_8 from UO_4 had more apparent change with increasing aging time. Nonetheless, α-U_3O_8 from AUC was found to hydrate more quickly than α-U_3O_8 from UO_4, which can likely be attributed to its larger surface area and porous starting material morphology.

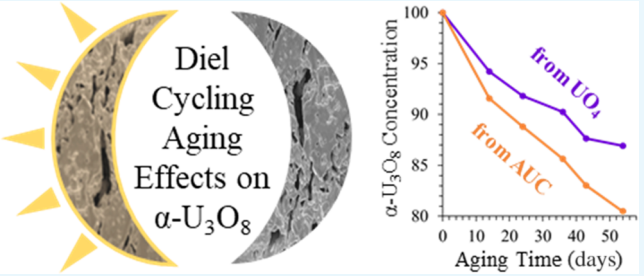

INTRODUCTION

Physical and chemical signatures of nuclear material vary throughout its lifecycle from ore processing to the long-term storage of nuclear fuel and represent a central focus of nuclear forensic investigations.[1] The provenance of nuclear material can be elucidated by signatures from industrial processes such as phase purity, synthetic route, precipitation conditions, thermal history, and the rate of oxidation.[2−5] Of additional interest in determining material origin are signatures from temporal processes resulting from changes in chemical speciation due to environmental conditions. Previous U-oxide aging studies have demonstrated the utility of morphologic signatures, quantitative crystallography, thermogravimetric analysis, spectroscopic techniques, isotopic ratios, and predictive modeling in determining material speciation as a result of storage conditions.[6−14] Each of these studies confirmed the formation of uranyl hydrate phases due to U-oxide aging.

U-oxides commonly found in the nuclear fuel cycle including UO_3, U_3O_8, and UO_2 are well known to undergo hydration to several uranyl oxide hydrate phases known as schoepites, which comprise the general formula $[(UO_2)_xO_y(OH)_z]^{(2x-2y-z)}$. Three phases commonly reported in the literature include schoepite, $UO_3{\cdot}xH_2O$, where $2 < x \leq 2.25$, metaschoepite, $UO_3{\cdot}2H_2O$, and paulscherrerite or "dehydrated schoepite", $UO_3{\cdot}xH_2O$ where $0.8 < x \leq 1$.[10,15,16] Additional phases closely related to schoepite include ianthinite, $(U^{4+})_2(UO_2)_4O_6(OH)_4{\cdot}9H_2O$, the only uranyl oxide hydrate phase recognized to contain U^{4+};[17] and paraschoepite, the existence of which has been debated. Paraschoepite was described by Christ and Clark as $5UO_3{\cdot}9.5H_2O$,[16,18] but was later hypothesized to be a mixture of metaschoepite, dehydrated schoepite, and ianthinite by Finch et al.[19]

Of particular interest in this study is the formation of uranyl oxide hydrate phases in relation to the synthetic route (i.e., the starting material) the aged material was prepared from. A variety of reagents can be utilized in uranium precipitation. In commercial processes, the choice of reagent is dependent on the desired purity, process efficiency, and economic, environmental, and safety concerns.[20,21] Two commonly used reagents are hydrogen peroxide, H_2O_2, and ammonium carbonate, $(NH_4)_2CO_3$. The uranium ore concentrates produced by the precipitation of uranyl nitrate with H_2O_2 (uranyl peroxide, $[(UO_2)O_2(H_2O)_2]{\cdot}2H_2O$, referred to throughout as UO_4) or

Received: May 11, 2021
Accepted: June 22, 2021
Published: July 7, 2021

$(NH_4)_2CO_3$ (ammonium uranyl carbonate, $(NH_4)_4[UO_2(CO_3)_3]$, AUC) are shown in eqs 1 and 2, respectively.[22]

$$UO_2(NO_3)_2 + H_2O_2 + 4H_2O \rightarrow [(UO_2)O_2(H_2O)_2 \cdot 2H_2O + 2HNO_3 \quad (1)$$

$$UO_2(NO_3)_2 + 3(NH_4)_2CO_3 \rightarrow (NH_4)_4[UO_2(CO_3)_3] + 2NH_4NO_3 \quad (2)$$

Previous work on synthetic route discernment by Schwerdt et al. quantitatively proved uranium ore concentrates, including UO_4 and AUC, and their subsequent calcination and reduction products have vastly different particle morphologies. Specifically, AUC, α-U_3O_8 from AUC, and UO_2 from AUC consist of monoclinic particles approximately an order of magnitude larger than their UO_4 counterparts, ultimately validating the use of morphology to determine starting material.[3] In another work by Sweet et al., various UO_3 polymorphs were prepared from UO_4 and AUC and aged under constant relative humidity (RH). Investigation through diffraction and spectroscopic techniques showed that the starting material, polymorphs, and hydration products can be used in determining the process history of UO_3.[4]

Additional aging studies utilizing multiple synthetic routes and cycling humidity to simulate more realistic aging conditions would be advantageous in predicting the fate of nuclear material. In this work, α-U_3O_8 was prepared via the washed UO_4 and AUC synthetic routes. Samples were stored under diel cycling conditions in a humidity chamber for a maximum of 54 days. The chamber operated on continuous daily cycles of 12 h "high" humidity and temperature, 45 °C and 90% RH, and 12 h "low," 25 °C and 20% RH. Powder X-ray diffraction (p-XRD) coupled with whole pattern fitting (WPF) in MDI Jade 9 software[23] was used for quantification of crystallographic changes. Scanning electron microscopy (SEM) with 12-way classification via machine learning was utilized for determining the discernability of the morphology between samples.

EXPERIMENTAL SECTION

Synthesis. The synthesis of α-U_3O_8 via the UO_4 and AUC synthetic routes was based on prior work by Olsen et al.[24] and Schwerdt et al.,[3] respectively. In the UO_4 synthetic route, UNH, $UO_2(NO_3)_2 \cdot 6H_2O$, was dissolved in deionized water (18.2 MΩ) to form a 0.1 M solution. Studtite, $(UO_2)O_2(H_2O)_2 \cdot 2H_2O$, was then synthesized as a precipitate by the dropwise addition of a molar excess of 30% hydrogen peroxide, H_2O_2. The solution was digested for 30 min and vacuum filtered at ambient temperature. The precipitate was washed with three 50 mL aliquots of deionized water to remove residual nitrates and allowed to dry at room temperature for 24 h. Subsequent drying at 80 °C for 24 h produced metastudtite, $(UO_2)(O_2)(H_2O)_2$, which was utilized as the starting material for calcination to α-U_3O_8.

In the AUC synthetic route, UNH was dissolved in deionized water to form a 0.5 M solution and heated to 40 °C at a stirring rate of 400 rpm. AUC was synthesized through the dropwise addition of 212 g/L ammonium carbonate, $(NH_4)_2CO_3$, to the UNH solution until pH 7.9 was reached. The solution was then allowed to digest for 30 min at 40 °C. The precipitate was vacuum filtered and washed with three 50 mL aliquots of 223 g/L ammonium carbonate and 50 mL of ethanol for removal of residual nitrates and allowed to dry at room temperature for 24 h.

The starting material from each synthetic route was placed separately into 5 mL platinum crucibles seated within aluminum oxide boats for calcination. The synthesis of α-U_3O_8 followed previous work by Tamasi et al.[9,10] Samples were held at a calcination temperature of 800 °C for 20 h under 500 mL/min of purified air to yield α-U_3O_8.

Aging Conditions. Following calcination to α-U_3O_8, samples were placed in 5 mL high-density polyethylene (HDPE) vials and immediately subjected to diel cycling storage conditions. Samples were aged in a MEMMERT GmbH + Co. KG HCP 108 L volume humidity chamber programmed for diel cycles of 12 "high" hours at 45 °C and 90% RH, and 12 "low" hours at 25 °C and 20% RH. These aging conditions were chosen to simulate a proof of concept day and night cycle, where the "high" temperature and humidity reflect the daytime settings and the "low" represent the nighttime settings. To prevent condensation on the instrument interior and sample vessels, the "high" humidity level was introduced after the chamber was stable at 45 °C for 30 min in each daily cycle.

Operating conditions within the chamber are uniform; temperature was controlled by large-area, all-round heating, with ±0.25 °C uniformity at diel cycling conditions. The temperature was measured using a Pt100 in a four-wire circuit and is accurate to 1 °C. Humidity was introduced into the chamber via a dry steam generator and deionized water. The water vapor is passed through a dosing pump and dispersed throughout the chamber by a fan. The humidity was measured by a capacitive humidity sensor and is accurate to 1% RH. Overall, the uniform, continuous atmosphere is guaranteed by a turbulence-free ventilation system within the chamber.[25]

Celsius 2007 software developed by MEMMERT GmbH + Co. KG was used for the analysis of the temperature and relative humidity values recorded by internal ring protocol memory.[26] There were no instances of power loss or any other anomalies for the full aging duration. Example achieved values for the diel cycle can be found in the Supporting Information. It should be noted that as the humidity chamber lacks cooling function, the "low" target temperature of 25 °C was never attained after 12 h, and averaged approximately 35.4 °C at the end of each cycle over the full aging duration.

Samples were aged at varying intervals for a maximum of 54 days. There was a total of five sampling times including 14, 24, 36, 43, and 54 days. Both synthetic routes were replicated in triplicate for a total of 30 samples. At each sampling interval, all samples were removed on the "low" cycle after at least 9 h had elapsed for that day to ensure consistency between sampling times. All replicates from both synthetic routes were removed from the humidity chamber at the same time for each interval, and samples were stored under vacuum at 24 in Hg when not being used for data analysis.

Powder X-ray Diffraction (p-XRD). Following aging, samples were prepared for p-XRD analysis by grinding with a high-purity aluminum oxide mortar and pestle and 2 mL of *n*-pentane. The material was then loaded on a P-type, B-doped silicon crystal zero diffraction plate. Characterization was performed on a Bruker D2 Phaser from 10 to 70° 2θ. Scans were recorded with a position-sensitive detector (PSD) opening of 5.01, 0.02° step size, 1.7 s/step, and 2965 steps for a total scan time of 91 min. A 0.6 mm divergence slit, 1 mm

https://doi.org/10.1021/acsomega.1c02487
ACS Omega 2021, 6, 18426−18433

antiscattering beam knife height, and 3 mm receiving slit were utilized. Samples were rotated at 15 rpm to account for any preferential orientation.

Quantitative analysis via WPF refinement was completed in MDI Jade 9.[23] Modeling parameters included background, specimen displacement, profile parameters, and phase parameters such as lattice constants, intensity scale factor, and full width at half-maximum (FWHM) for corrected peak positions. Reference patterns were obtained from the PDF-4+ 2020 database[27] and the NIST ICSD.[28]

Scanning Electron Microscopy (SEM). SEM samples were prepared prior to grinding for p-XRD analysis. Typically, 5−10 mg of each sample was dispersed onto a 12 mm conductive carbon tab fixed to a 12.7 mm aluminum pin stub mount. Each pin was lightly tapped to remove any loose material and coated with approximately 200 Å of Au/Pd film to prevent excessive surface charging. Images were acquired by a FEI Nova NanoSEM 630 high-resolution scanning electron microscope. The through the lens (TLD) secondary electron (SE) detector was used at an accelerating voltage of 5 kV. All images were taken at 25 000× magnification for qualitative comparison of the morphology.

Machine Learning. Convolutional neural networks (CNN) are deep learning algorithms that have previously demonstrated a great ability to discriminate between uranium ore concentrate synthetic route, calcination conditions, and coprecipitated impurities.[2,29−31] As training CNNs from scratch is time consuming and requires a large amount of image data, it is often beneficial to perform transfer learning, in which a model that has been pretrained on another data set is fine-tuned to a new set of images; the Resnet34 architecture pretrained with ImageNet weights was the starting model.[32,33] The top of the model was replaced for 12-way classification, with labels corresponding to the unaged controls and the five aging lengths for both synthetic routes. The Keras deep learning API (version 2.3.1)[34] with the TensorFlow backend (version 2.1.0)[35] for Python (version 3.7.7)[36] were used to fit and evaluate the classifiers, using a single NVIDIA RTX 2060 (6 GB) for graphics processing unit (GPU)-accelerated computing.

The data set consisted of 964 micrographs with resolutions of 1024 × 884 pixels excluding the information bar at the bottom of the image. Each class had approximately 90 images, with the exception of unaged controls, which each had about 30 images. Eighty percent of the images were used to train and validate the classifier, while the remaining 20% were designated as the test set. Within the training set, the unaged image data was oversampled to provide nearly equal class sizes. To increase the number of images available for training and classification, the full-sized images placed in either split were used to create five 512 × 442 pixel crops from the four corners and center of the image.

Fivefold cross-validation (CV) is a method that establishes train and validation folds from the training split, and then trains and evaluates the model on alternating folds to obtain a mean classification accuracy and uncertainty. Fivefold CV was used to determine hyperparameters (number of training epochs, learning rates, etc.) that resulted in the best classifier performance. During training and validation images were augmented by flipping images across the horizontal and/or vertical axis, then randomly cropping to 224 × 224 pixels (the input size of the Resnet34 architecture). The final model had a fivefold CV accuracy of 92.0 ± 0.8%. Additional details on selecting the final model are presented in the Supporting Information. After cross-validation, the model was trained using the same parameters but with all of the training set data, which was used to make predictions on 224 × 224 pixel crops at the center of the test set images.

RESULTS AND DISCUSSION

Powder X-ray Diffraction (p-XRD). The crystalline composition of all samples was determined by p-XRD analysis, while the classification and proceeding WPF was completed using Jade. The normalized intensity spectra of aged α-U_3O_8 from UO_4 and AUC synthetic routes are shown in Figures 1 and 2, respectively. Aging times of 14, 24, 36, 43, and 54 days are compared against the control and reference patterns for ianthinite, metaschoepite, and α-U_3O_8. Figure 1 is representative of aged α-U_3O_8 samples from the UO_4 synthetic route and illustrates the increase of ianthinite and metaschoepite formation as aging time increases. Metaschoepite, $UO_3 \cdot 2H_2O$, has the most significant peak at 12.1° (2θ) and overlaps with ianthinite, $(U^{4+})_2(UO_2)_4O_6(OH)_4 \cdot 9H_2O$, with the most significant peak at 11.6° (2θ). While ianthinite formation was qualitatively low, the 11.6° (2θ) peak can be observed by the broadening of the left side of the 12.1° (2θ) metaschoepite peak.

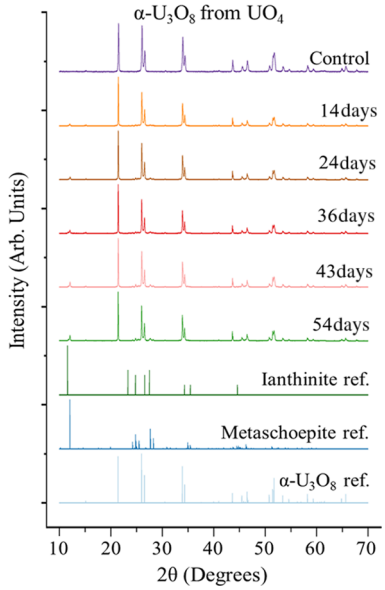

Figure 1. p-XRD spectra comparison of α-U_3O_8 from the UO_4 synthetic route. The spectrum representative of the unaged control is shown at the top of the graph, followed by spectra characteristic of samples aged 14, 24, 36, 43, and 54 days, respectively. The reference patterns for ianthinite (ICSD #84442), metaschoepite (ICSD #76895), and α-U_3O_8 (PDF #04-007-1246) are included at the bottom of the graph.

Figure 2 represents the aged α-U_3O_8 samples from the AUC synthetic route. In agreement with the α-U_3O_8 from UO_4 samples, there is a qualitative increase in ianthinite and metaschoepite formation as the aging time increases from 14 to 54 days. Additionally, α-U_3O_8 from AUC appears to form a qualitatively greater amount of schoepite phases compared to α-U_3O_8 from UO_4 as shown by the larger 11.6 and 12.1° (2θ) peak intensities at each aging interval, suggesting that α-U_3O_8 from AUC hydrates more quickly. Comparative spectra figures

https://doi.org/10.1021/acsomega.1c02487
ACS Omega 2021, 6, 18426−18433

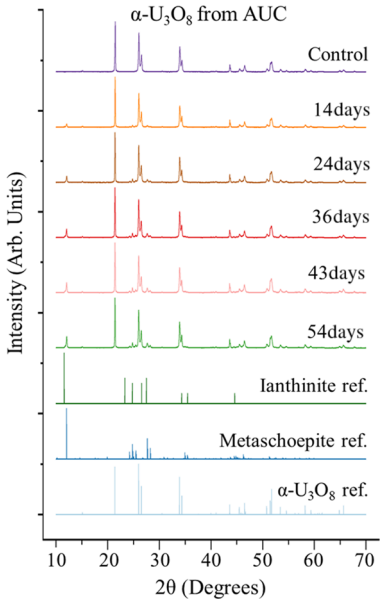

Figure 2. p-XRD spectra comparison of α-U_3O_8 from the AUC synthetic route. The spectrum representative of the unaged control is shown at the top of the graph, followed by spectra characteristic of samples aged 14, 24, 36, 43, and 54 days, respectively. The reference patterns for ianthinite (ICSD #84442), metaschoepite (ICSD # 76895), and α-U_3O_8 (PDF #04-007-1246) are included at the bottom of the graph.

for sample replicates at each aging interval can be found in the Supporting Information.

As U_3O_8 contains approximately 70% U^{5+} and 30% U^{6+}, the formation of ianthinite containing the U^{4+} oxidation state indicates that the aged samples must have either been exposed to a reducing environment or undergone a disproportionation reaction.[37,38] In uranium disproportionation, two U^{5+} ions disproportionate to form one U^{4+} ion and one U^{6+} ion.[39−41] However, the specific conditions of ianthinite formation have not been well described. Previous work by Taylor et al. found evidence of ianthinite formation when oxidizing UO_2 at 200 °C due to oxygen depletion in sealed reaction vessels,[42] while a long-term α-U_3O_8 aging study by Tamasi et al. used Swagelok fittings for sealed reaction vessels and saw no formation of ianthinite.[10] Other work by Oerter et al. utilized humidity chambers to expose α-U_3O_8 to constant humidity levels over 180 days and additionally reported no formation of ianthinite. However, air was circulated through each chamber at 500 cm^3/min.[7]

In this study, samples were left unsealed and open to the humidity chamber atmosphere for the full aging duration and were stored under vacuum when not being used for analysis. It is therefore unlikely ianthinite formed due to oxygen depletion in sealed vessels. As the humidity chamber is equipped with a ventilation system, it is additionally unlikely that inadequate aeration caused a partially reducing environment, albeit continuous air flow of the chamber was not monitored throughout the experiment. It is possible that U^{5+} disproportionated on the high temperature and humidity cycles and reprecipitated on low cycles to form U^{4+} and U^{6+}. These observations illustrate the importance and challenge of replicating realistic aging conditions in a laboratory setting. Furthermore, as ianthinite is known to be unstable at ambient conditions and readily oxidizes to form schoepite and metaschoepite, these results show the importance of using rapid analytical techniques for forensic analyses.

Whole Pattern Fitting (WPF) of Aged p-XRD Spectra. Quantitative analysis via WPF refinement in Jade was pursued to establish a statistical difference between samples as aging time increases and between synthetic routes. The WPF refinement method, also known as the Pawley method,[43] uses a nonlinear least-square approach to optimize the observed data to a modeled pattern and calculate the weight percent of each phase. The quality of each refinement was measured by the difference profile plot and the computed agreement indices R and E, where R compares the calculated pattern to the observed pattern and E represents the quality of the data. R/E was additionally calculated and represents the goodness of fit (GOF), which theoretically approaches 1 in an ideal refinement.[23,44] R, E, and GOF values for each sample refinement can be found in the Supporting Information.

Comprehensive results from the refinement are shown in Table 1, and the degradation of α-U_3O_8 as well as metaschoepite and ianthinite formation are illustrated in Figures 3 and 4, respectively. Results are reported as averages ± the error, 1σ. It should be noted that in some instances, the

Table 1. WPF Refinement Results for All Samples[a]

material	aging time (days)	metaschoepite (wt %)	ianthinite (wt %)	α-U_3O_8 (wt %)
α-U_3O_8 from UO_4	14	3.4 ± 0.4	2.3 ± 0.4	94.2 ± 0.4
	24	4.73 ± 0.05	3.43 ± 0.09	91.8 ± 0.1
	36	5.7 ± 0.6	4.0 ± 0.6	90.27 ± 0.05
	43	7.7 ± 0.7	4.7 ± 0.6	87.6 ± 0.7
	54	8.0 ± 0.3	5.0 ± 0.1	86.9 ± 0.4
α-U_3O_8 from AUC	14	4.8 ± 0.5	3.6 ± 0.4	91.6 ± 0.3
	24	7.2 ± 0.5	4.0 ± 0.6	88.8 ± 0.8
	36	9.23 ± 0.05	5.1 ± 0.2	85.6 ± 0.2
	43	11.7 ± 0.4	5.3 ± 0.4	83.0 ± 0.5
	54	12 ± 1	7.1 ± 0.4	80.5 ± 0.6

[a]Metaschoepite, ianthinite, and α-U_3O_8 values are given as the average for each sample ± the error, 1σ. α-U_3O_8 from AUC quantitatively appears to age more quickly than α-U_3O_8 from UO_4.

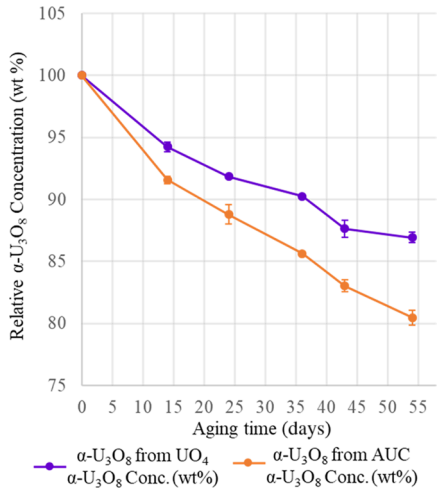

Figure 3. Decrease of α-U_3O_8 concentration as aging time increases. α-U_3O_8 from UO_4 is shown in purple, while α-U_3O_8 from AUC is shown in orange. Results are illustrated as averages ± the error, 1σ. α-U_3O_8 from AUC hydrated more quickly than α-U_3O_8 from UO_4.

https://doi.org/10.1021/acsomega.1c02487
ACS Omega 2021, 6, 18426−18433

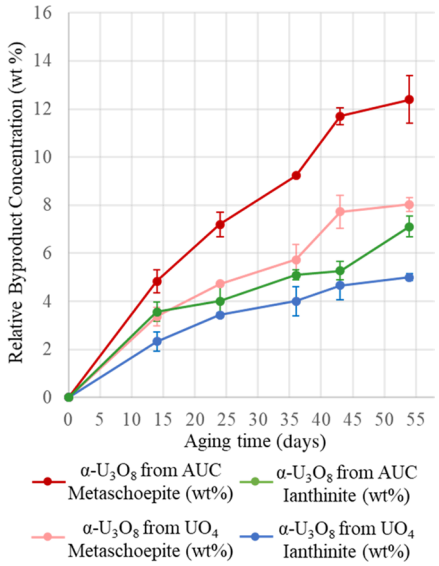

Figure 4. Increasing metaschoepite and ianthinite concentration as aging time increases. The relative byproduct (metaschoepite and ianthinite) concentrations in α-U_3O_8 from AUC are shown by the red and green lines, respectively, and the byproduct concentrations in α-U_3O_8 from UO_4 are shown by the pink and blue lines, respectively. α-U_3O_8 from AUC hydrated more quickly than α-U_3O_8 from UO_4.

error is too minimal to be observed in Figures 3 and 4; however, error values for all data points can be found in Table 1. In correlation with the qualitative p-XRD results, α-U_3O_8 from AUC hydrated more quickly than α-U_3O_8 from UO_4 as observed by the greater degradation of α-U_3O_8 from AUC with increasing aging time (Figure 3). This is further supported by Figure 4, which shows that α-U_3O_8 from AUC had a greater formation of metaschoepite and ianthinite than α-U_3O_8 from UO_4 as aging time increased. At each aging interval, α-U_3O_8, metaschoepite, and ianthinite phases were quantifiably distinguishable at 1σ error between synthetic routes.

Similarly, α-U_3O_8 from UO_4 samples had quantifiably discernable α-U_3O_8 concentrations between aging intervals. However, metaschoepite concentration was not distinguishable at 1σ error between 43 and 54 day aging times, while ianthinite concentration was not distinguishable between 36 and 43, nor 43 and 54 days aging times. α-U_3O_8 from AUC additionally had differentiable α-U_3O_8 concentrations between aging times but did not have discernable metaschoepite concentration between 43 and 54 day samples. Ianthinite concentration was not discernable between any sequential aging intervals (i.e., 14−24, 24−36 days, etc.) with the exception of the 43−54 days interval. Nonetheless, all samples show a clear increase in metaschoepite and ianthinite concentration throughout the aging duration in correspondence with the degradation of α-U_3O_8.

As α-U_3O_8 concentration was quantifiably differentiable between all samples at all aging intervals, the indiscernibility of metaschoepite and ianthinite phase concentrations is likely explained by the overlap of their most significant diffraction peaks as well as their overall low concentrations and correspondingly low intensities; the accuracy of the refinement is dependent upon the counting time and the number of steps over each peak, where each step signifies a discrete measurement contributing to the total intensity, and the amount of reflection overlap.[44]

Nonetheless, the quantifiably greater hydrolysis of α-U_3O_8 from AUC signifies the importance of normalizing starting material to rate of hydration. Previous catalytic oxidation studies have proven that, in some cases, increased surface area and surface defects result in higher reaction rates.[45,46] We hypothesize that the faster rate of hydrolysis of α-U_3O_8 from AUC is attributed to its larger surface area and larger, porous particle morphology. Future studies comparing starting material surface area to rate of hydrolysis are essential to developing predictive, individual aging models specific to starting morphology.

Scanning Electron Microscopy (SEM). SEM imagery was collected for each sample to evaluate the α-U_3O_8 surface morphology changes over time and to continue expanding the U-oxide morphological data set. Over 900 SEM images were taken for analysis. A lexicon developed by Tamasi et al. for maintaining consistent descriptors of nuclear material morphology was used to qualitatively evaluate each sample.[47] Figure 5 illustrates the qualitative changes between samples as aging time increases.

The α-U_3O_8 from the UO_4 control sample morphology parallels previously published descriptors.[2,9,24] The sample is comprised of clumped/massive agglomerates with rounded/subrounded particles and semirounded grains. The surface features are somewhat smooth. However, as aging time increases, the grains become more dissimilar in their sizes and morphology, resulting in clumped conglomerates of particles. Additionally, individual microparticles/grains become much sparser and change from semirounded to subangular in shape. Additionally, the surface features become somewhat rough in texture.

The control sample morphology of α-U_3O_8 from aligns with previous work in which the α-U_3O_8 from AUC was synthesized under the same conditions.[3] Overall, the particle morphology of α-U_3O_8 from AUC is much larger than α-U_3O_8 from UO_4. The control sample contains clumped/massive conglomerates with angular, blocky particles. The surface is somewhat smooth and contains pores due to the release of gases such as carbon dioxide, water, or ammonia as AUC dissociates to α-U_3O_8.[48−51] As the aging time increases, the overall particle morphology remains the same, that is, clumped/massive conglomerates with angular, blocky particles. The surface maintains pores but becomes somewhat rough in appearance. Overall, aged α-U_3O_8 from both UO_4 and AUC are qualitatively discernable from their corresponding controls. This compliments the p-XRD data, which showed the formation of metaschoepite and ianthinite as the α-U_3O_8 aged.

Machine Learning. In past morphology studies, SEM imagery has been manually quantified via Morphological Analysis of MAterials (MAMA) software developed by Los Alamos National Laboratory.[2,3,5,11,24,29−31,52−54] This software can be highly useful for quantitatively distinguishing sample morphology via particle attributes such as pixel area, circularity, and ellipse aspect ratio. However, successful MAMA analyses rely on the ability to manually segment individual, unobscured particles within the imagery. While the α-U_3O_8 from UO_4 control contains discrete particles, these features became increasingly infrequent as the material aged. Moreover, α-U_3O_8 from AUC contains no discrete particles in the control nor the aged samples. In cases when manual segmentation is not possible, automated machine learning can provide a viable alternative. Therefore, machine learning analysis via 12-way classification was pursued to establish whether or not the aged

https://doi.org/10.1021/acsomega.1c02487
ACS Omega 2021, 6, 18426−18433

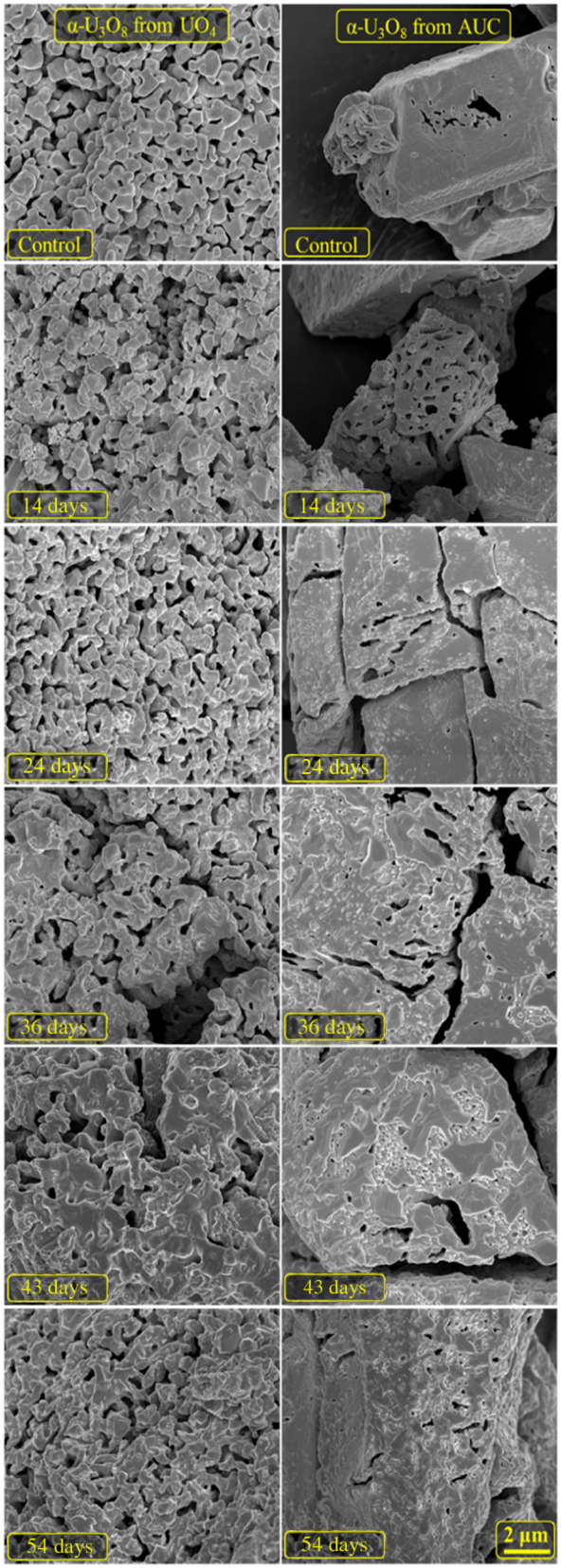

Figure 5. SEM image comparison between samples and the synthetic route as aging time increases. α-U_3O_8 from UO_4 is shown in the left column, while α-U_3O_8 from AUC is shown in the right. The imagery of the control samples is shown in the first row, followed by aging times of 14, 24, 36, 43, and 54 days. All images are on the same scale.

materials had surface morphologies that could be distinguished from one another. Due to the blackbox nature of CNNs, little can be definitively said about the features used by the network to make its classification decisions, though research into explainable artificial intelligence (XAI) is seeking to make advances on this front.

The overall classification accuracy of the test set images was 93.2%, with 895 of the 960 five-way partitioned image crops correctly predicted. Figure 6 shows a confusion matrix

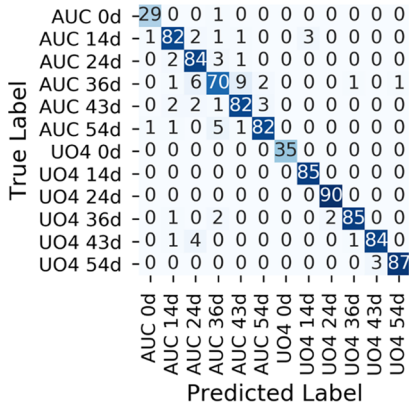

Figure 6. Confusion matrix indicating which image classes were most frequently predicted as one another. True labels are illustrated by the *Y*-axis, while predicted labels are shown on the *X*-axis. The greatest confusion was between α-U_3O_8 from AUC materials with aging times of 24 days or longer.

indicating which image classes were most frequently predicted for each label. In general, α-U_3O_8 from the UO_4 synthetic route saw more accurate predictions than those from the AUC synthetic route. This likely reflects the change in morphology of α-U_3O_8 from UO_4: the somewhat-smooth rounded or subrounded agglomeration of grains for the unaged α-U_3O_8 transitioned to subangular conglomerations of grains with rougher surface features with longer aging times. The confusion matrix shows rare misclassifications of aged α-U_3O_8 from UO_4 materials, mostly between adjacent aging times, but also occasionally with aged α-U_3O_8 from AUC classes.

In contrast, the aged α-U_3O_8 from AUC saw notably more misclassified examples between aged classes, particularly with aging times between 24 and 43 days. This trend is likely explained by the overall surface morphology characteristics undergoing less change over time with respect to α-U_3O_8 from UO_4; the grains became rougher, but the bulk angular, blocky particle morphology remained the same. Nonetheless, different aging times for AUC could be reasonably predicted by the classifier. No clear trend in classifier performance was seen as a function of aging time as measured by precision, recall, and f-measure, which may indicate that an equilibrium with respect to surface morphology changes had not yet been reached by 54 days of aging as the trained classifier was able to discriminate between aging times.

CONCLUSIONS

In this work, α-U_3O_8 was synthesized via UO_4 and AUC synthetic routes and stored under diel cycling relative humidity and temperature. p-XRD with quantitative WPF illustrated the dissociation of α-U_3O_8 over the course of 14, 24, 36, 43, and 54 day sampling times. The formation of metaschoepite and

https://doi.org/10.1021/acsomega.1c02487
ACS Omega 2021, 6, 18426−18433

ianthinite was observed in all aged samples. Overall, α-U_3O_8 from AUC hydrated more quickly than α-U_3O_8 from UO_4, likely due to its larger surface area and larger, porous particle morphology. SEM imagery complemented by 12-way classification via machine learning indicated that all samples had unique morphologic characteristics, though more apparent changes were seen in the α-U_3O_8 from UO_4 samples. Overall, this study advances the knowledge of U-oxide speciation as a product of synthetic route and environmental conditions, giving novel insight to determining the provenance of nuclear material.

■ ASSOCIATED CONTENT

Supporting Information

The Supporting Information is available free of charge at https://pubs.acs.org/doi/10.1021/acsomega.1c02487.

Expected and observed error and GOF values from WPF; precision, recall, and F1 scores from the 12-way classification; Example observed HCP temperature and humidity values over 6 days; Normalized p-XRD spectra comparison for all sample replicates; additional SEM imagery comparison between aging times; and additional information for CNN image classification (PDF)

■ AUTHOR INFORMATION

Corresponding Author

Luther W. McDonald, IV − *Department of Civil and Environmental Engineering, Nuclear Engineering Program, University of Utah, Salt Lake City, Utah 84112, United States;* orcid.org/0000-0001-6735-5410; Phone: 1-801-581-7768; Email: luther.mcdonald@utah.edu

Authors

Alexa B. Hanson − *Department of Civil and Environmental Engineering, Nuclear Engineering Program, University of Utah, Salt Lake City, Utah 84112, United States*

Cody A. Nizinski − *Department of Civil and Environmental Engineering, Nuclear Engineering Program, University of Utah, Salt Lake City, Utah 84112, United States*

Complete contact information is available at: https://pubs.acs.org/10.1021/acsomega.1c02487

Author Contributions

The manuscript was written through the contributions of all authors. All authors have given approval to the final version of the manuscript.

Notes

The authors declare no competing financial interest.

■ ACKNOWLEDGMENTS

The synthesis, aging, and characterization of α-U_3O_8 samples were supported by the U.S. Department of Homeland Security, Domestic Nuclear Detection Office, under Grant award no. 2015-DN-077-ARI092. The same DHS grant, along with the Defense Threat Reduction Agency, under Grant award no. HDTRA1-16-1-0026 supported the quantitative morphological analysis via machine learning. The views and conclusions contained in this document are those of the authors and should not be interpreted as necessarily representing the official policies, either expressed or implied, of the U.S. Department of Homeland Security or Defense Threat Reduction Agency. This work made use of University of Utah Shared facilities of the Surface Analysis and Nanoscale Imaging Group sponsored by the College of Engineering, Health Sciences Center, Office of the Vice President for Research, and the Utah Science Technology and Research (USTAR) Initiative of the State of Utah.

■ REFERENCES

(1) Mayer, K.; Wallenius, M.; Varga, Z. Nuclear Forensic Science: Correlating Measurable Material Parameters to the History of Nuclear Material. *Chem. Rev.* **2013**, *113*, 884−900.

(2) Hanson, A. B.; Lee, R. N.; Vachet, C.; Schwerdt, I. J.; Tasdizen, T.; McDonald, L. W. Quantifying Impurity Effects on the Surface Morphology of α-U_3O_8. *Anal. Chem.* **2019**, *91*, 10081−10087.

(3) Schwerdt, I. J.; Hawkins, C. G.; Taylor, B.; Brenkmann, A.; Martinson, S.; McDonald, L. W., IV Uranium Oxide Synthetic Pathway Discernment through Thermal Decomposition and Morphological Analysis. *Radiochim. Acta* **2019**, *107*, 193−205.

(4) Sweet, L. E.; Blake, T. A.; Henager, C. H.; Hu, S.; Johnson, T. J.; Meier, D. E.; Peper, S. M.; Schwantes, J. M. Investigation of the Polymorphs and Hydrolysis of Uranium Trioxide. *J. Radioanal. Nucl. Chem.* **2013**, *296*, 105−110.

(5) Olsen, A. M.; Schwerdt, I. J.; Richards, B.; McDonald, L. W. Quantification of High Temperature Oxidation of U_3O_8 and UO_2. *J. Nucl. Mater.* **2018**, *508*, 574−582.

(6) Scott, D. B.; Dai, Z. R.; Davisson, M. L.; Jeffries, J. R.; Nelson, A. J. An XPS Study on the Impact of Relative Humidity on the Aging of UO_2 Powders. *J. Nucl. Mater.* **2017**, *487*, 105−112.

(7) Oerter, E. J.; Singleton, M.; Dai, Z.; Deinhart, A.; Thaw, M.; Davisson, M. L. Hydrogen and Oxygen Stable Isotope Composition of Water in Metaschoepite Mineralization on U_3O_8. *Appl. Geochem.* **2020**, *112*, No. 104469.

(8) Oerter, E. J.; Singleton, M.; Davisson, M. L. Hydrogen and Oxygen Stable Isotope Dynamics of Hyper-Saline and Salt-Saturated Aqueous Solutions. *Geochim. Cosmochim. Acta* **2018**, *238*, 316−328.

(9) Tamasi, A. L.; Cash, L. J.; Mullen, W. T.; Pugmire, A. L.; Ross, A. R.; Ruggiero, C. E.; Scott, B. L.; Wagner, G. L.; Walensky, J. R.; Wilkerson, M. P. Morphology of U_3O_8 Materials Following Storage under Controlled Conditions of Temperature and Relative Humidity. *J. Radioanal. Nucl. Chem.* **2017**, *311*, 35−42.

(10) Tamasi, A. L.; Boland, K. S.; Czerwinski, K.; Ellis, J. K.; Kozimor, S. A.; Martin, R. L.; Pugmire, A. L.; Reilly, D.; Scott, B. L.; Sutton, A. D.; Wagner, G. L.; Walensky, J. R.; Wilkerson, M. P. Oxidation and Hydration of U_3O_8 Materials Following Controlled Exposure to Temperature and Humidity. *Anal. Chem.* **2015**, *87*, 4210−4217.

(11) Hanson, A. B.; Schwerdt, I. J.; Nizinski, C. A.; Lee, R. N.; Mecham, N. J.; Abbott, E. C.; Heffernan, S.; Olsen, A.; Klosterman, M. R.; Martinson, S.; Brenkmann, A.; McDonald, L. W. Impact of Controlled Storage Conditions on the Hydrolysis and Surface Morphology of Amorphous-UO_3. *ACS Omega* **2021**, *6*, 8605−8615.

(12) Pastoor, K. J.; Robinson, S. L.; Greenwell, R. A.; Quintero Hilsaca, C. V.; Shafer, J. C.; Jensen, M. P. Understanding Uranium Oxide Hardening during Prolonged Storage. *Radiochim. Acta* **2020**, *108*, 943−953.

(13) Wilkerson, M. P.; Hernandez, S. C.; Mullen, W. T.; Nelson, A. T.; Pugmire, A. L.; Scott, B. L.; Sooby, E. S.; Tamasi, A. L.; Wagner, G. L.; Walensky, J. R. Hydration of α-UO_3 Following Storage under Controlled Conditions of Temperature and Relative Humidity. *Dalton Trans.* **2020**, *49*, 10452−10462.

(14) Reilly, D. Molecular Forensic Science Analysis of Nuclear Materials. University of Nevada, 2012.

(15) Wheeler, V. J.; Dell, R. M.; Wait, E. Uranium Trioxide and the UO_3 Hydrates. *J. Inorg. Nucl. Chem.* **1964**, *26*, 1829−1845.

(16) Brugger, J.; Meisser, N.; Etschmann, B.; Ansermet, S.; Pring, A. Paulscherrerite from the Number 2 Workings, Mount Painter Inlier, Northern Flinders Ranges, South Australia: "Dehydrated Schoepite" Is a Mineral after All. *Am. Mineral.* **2011**, *96*, 229−240.

(17) Burns, P. C.; Finch, R. J.; Hawthorne, F. C.; Miller, M. L.; Ewing, R. C. The Crystal Structure of Ianthinite, $[U^{4+}(UO_2)_4O_6(OH)_4(H_2O)_4](H_2O)_5$: A Possible Phase for Pu^{4+} Incorporation during the Oxidation of Spent Nuclear Fuel. *J. Nucl. Mater.* **1997**, *249*, 199−206.
(18) Christ, C. L.; Clark, J. R. Crystal Chemical Studies of Some Uranyl Oxide Hydrates. *Am. Mineral.* **1960**, *45*, 1026−1061.
(19) Finch, R. J.; Hawthorne, F. C.; Ewing, R. C. Structural Relations among Schoepite, Metaschoepite and "Dehydrated Schoepite. *Can. Mineral.* **1998**, *36*, 831−845.
(20) *Uranium Extraction Technology*; International Atomic Energy Agency, 1993.
(21) Edwards, C. R.; Oliver, A. J. Uranium Processing: A Review of Current Methods and Technology. *JOM* **2000**, *52*, 12−20.
(22) Cordfunke, E. H. P. *The Chemistry of Uranium: Including Its Applications in Nuclear Technology*; 1970.
(23) MDI Jade 9 (MDI), 2017.
(24) Olsen, A. M.; Richards, B.; Schwerdt, I.; Heffernan, S.; Lusk, R.; Smith, B.; Jurrus, E.; Ruggiero, C.; McDonald, L. W. Quantifying Morphological Features of α-U_3O_8 with Image Analysis for Nuclear Forensics. *Anal. Chem.* **2017**, *89*, 3177−3183.
(25) Memmert GmbH + Co. KG. D10345 Operating Instructions: Humidity Chambers HCP 108/153/246, 2017.
(26) Memmert GmbH + Co. KG. Celsius 10.0 Control Software for MEMMERT Appliances, 2017.
(27) *PDF-4+*; International Centre for Diffraction Data, 2020.
(28) *NIST Inorganic Crystal Structure Database*, NIST StandardReference Database Number 3; National Institute of Standards and Technology: Gaithersburg, 2021.
(29) Abbott, E. C.; Brenkmann, A.; Galbraith, C.; Ong, J.; Schwerdt, I. J.; Albrecht, B. D.; Tasdizen, T.; McDonald, L. W., IV Dependence of UO_2 Surface Morphology on Processing History within a Single Synthetic Route. *Radiochim. Acta* **2019**, *107*, 1121−1131.
(30) Schwerdt, I. J.; Brenkmann, A.; Martinson, S.; Albrecht, B. D.; Heffernan, S.; Klosterman, M. R.; Kirkham, T.; Tasdizen, T.; McDonald, L. W., IV Nuclear Proliferomics: A New Field of Study to Identify Signatures of Nuclear Materials as Demonstrated on Alpha-UO_3. *Talanta* **2018**, *186*, 433−444.
(31) Nizinski, C.; Hanson, A.; Fullmer, B.; Mecham, N.; Tasdizen, T.; McDonald, L., IV Effects of Process History on the Surface Morphology of Uranium Ore Concentrates Extracted from Ore. *Miner. Eng.* **2020**, No. 106457.
(32) He, K.; Zhang, X.; Ren, S.; Sun, J. In *Deep Residual Learning for Image Recognition*, 2016 IEEE Conference on Computer Vision and Pattern Recognition (CVPR), 2016; pp 770−778.
(33) Krizhevsky, A.; Sutskever, I.; Hinton, G. E. ImageNet Classification with Deep Convolutional Neural Networks. *Commun. ACM* **2017**, 84−90.
(34) Chollet, F.et al. Keras. https://keras.io.
(35) Abadi, M.; Barham, P.; Chen, J.; Chen, Z.; Davis, A.; Dean, J.; Devin, M.; Ghemawat, S.; Irving, G.; Isard, M.; Kudlur, M.; Levenberg, J.; Monga, R.; Moore, S.; Murray, D. G.; Steiner, B.; Tucker, P.; Vasudevan, V.; Warden, P.; Wicke, M.; Yu, Y.; Zheng, X. *TensorFlow: Large-Scale Machine Learning on Heterogeneous Systems*, 2015.
(36) Python Software Foundation. *Python Language Reference*, version 3.7.7; Python Software Foundation, 2020.
(37) Sanyal, K.; Khooha, A.; Das, G.; Tiwari, M. K.; Misra, N. L. Direct Determination of Oxidation States of Uranium in Mixed-ValentUranium Oxides Using Total Reflection X-ray Fluorescence X-rayAbsorption Near-Edge Spectroscopy. *Anal. Chem.* **2017**, *89*, 871−876.
(38) Kvashnina, K. O.; Butorin, S. M.; Martin, P.; Glatzel, P. Chemical State of Complex Uranium Oxides. *Phys. Rev. Lett.* **2013**, *111*, No. 253002.
(39) Kern, D. M. H.; Orlemann, E. F. The Potential of the Uranium (V), Uranium (VI) Couple and the Kinetics of Uranium (V) Disproportionation in Perchlorate Media. *J. Am. Chem. Soc.* **1949**, *71*, 2102−2106.
(40) Renshaw, J. C.; Butchins, L. J. C.; Livens, F. R.; Iain, M.; Charnock, J. M.; Llyod, J. R. Bioreduction of Uranium: Environmental Implications of a Pentavalent Intermediate. *Environ. Sci. Technol.* **2005**, *39*, 5657−5660.
(41) Yuan, K.; Renock, D.; Ewing, R. C.; Becker, U. Uranium Reduction on Magnetite: Probing for Pentavalent Uranium Using Electrochemical Methods. *Geochim. Cosmochim. Acta* **2015**, *156*, 194−206.
(42) Taylor, P.; Wood, D. D.; Owen, D. G.; Park, G.-I. Crystallization of U_3O_8 and Hydrated UO_3 on UO_2 Fuel in Aerated Water near 200 °C. *J. Nucl. Mater.* **1981**, *183*, 105−114.
(43) Pawley, G. S. Unit-Cell Refinement from Powder Diffraction Scans. *J. Appl. Crystallogr.* **1981**, *14*, 357−361.
(44) Mccusker, L. B.; Von Dreele, R. B.; Cox, D. E.; Louër, D.; Scardi, P. Rietveld Refinement Guidelines. *J. Appl. Crystallogr.* **1999**, *32*, 36−50.
(45) Ottone, C.; Armandi, M.; Hernández, S.; Bensaid, S.; Fontana, M.; Pirri, C. F.; Saracco, G.; Garrone, E.; Bonelli, B. Effect of Surface Area on the Rate of Photocatalytic Water Oxidation as Promoted by Different Manganese Oxides. *Chem. Eng. J.* **2015**, *278*, 36−45.
(46) Liu, Y.; Liu, Y.; Guo, Y.; Junwei, X.; Xianglan, X.; Fang, X.; Liu, J.; Chen, W.; Arandiyan, H.; Wang, X. Tuning SnO_2 Surface Area for Catalytic Toluene Deep Oxidation: On the Inherent Factors Determining the Reactivity. *Ind. Eng. Chem. Res.* **2018**, *57*, 14052−14063.
(47) Tamasi, A. L.; Cash, L. J.; Eley, C.; Porter, R. B.; Pugmire, D. L.; Ross, A. R.; Ruggiero, C. E.; Tandon, L.; Wagner, G. L.; Walensky, J. R.; Wall, A. D.; Wilkerson, M. P. A Lexicon for Consistent Description of Material Images for Nuclear Forensics. *J. Radioanal. Nucl. Chem.* **2016**, *307*, 1611−1619.
(48) Yi-Ming, P.; Che-Bao, M.; Nien-Nan, H. The Conversion of UO_2 via Ammonium Uranyl Carbonate: Study of Precipitation, Chemical Variation and Powder Properties. *J. Nucl. Mater.* **1981**, *99*, 135−147.
(49) Marajofsky, A.; Perez, L.; Celora, J. On the Dependence of Characteristics of Powders on the AUC Process Parameters. *J. Nucl. Mater.* **1991**, *178*, 143−151.
(50) Woolfrey, J. L. The Preparation of UO_2 Powder: Effect of Ammonium Uranate Properties. *J. Nucl. Mater.* **1978**, *74*, 123−131.
(51) Doi, H.; Ito, T. Significance of Physical State of Starting Precipitate in Growth of Uranium Dioxide Particles. *J. Nucl. Mater.* **1964**, *11*, 94−106.
(52) Ruggiero, C. E.; Bloch, J. J. *Morphological Analysis for Material Attribution (MAMA)*, version 2.1; Los Alamos National Laboratory, 2016.
(53) Schwerdt, I. J.; Olsen, A.; Lusk, R.; Heffernan, S.; Klosterman, M.; Collins, B.; Martinson, S.; Kirkham, T.; McDonald, L. W., IV Nuclear Forensics Investigation of Morphological Signatures in the Thermal Decomposition of Uranyl Peroxide. *Talanta* **2018**, *176*, 284−292.
(54) Heffernan, S. T.; Ly, N.-C.; Mower, B. J.; Vachet, C.; Schwerdt, I. J.; Tasdizen, T.; McDonald, L. W., IV Identifying Surface Morphological Characteristics to Differentiate between Mixtures of U_3O_8 Synthesized from Ammonium Diuranate and Uranyl Peroxide. *Radiochim. Acta* **2019**, *108*, 29−36.

https://doi.org/10.1021/acsomega.1c02487
ACS Omega 2021, 6, 18426−18433